Available online at www.sciencedirect.com
ScienceDirect
Cement & Concrete Composites 29 (2007) 313–323
Cement & Concrete Composites
www.elsevier.com/locate/cemconcomp

Gradient structures in cementitious materials

P. Stroeven *, J. Hu

Faculty of Civil Engineering and Geosciences, Delft University of Technology, Stevinweg 1, 2628 CN Delft, The Netherlands

Received 25 February 2006; accepted 1 October 2006
Available online 26 January 2007

Abstract

A methodological approach to gradient structures in concrete technology is outlined in this paper. It is introduced by summarizing the approach to bulk structures, because of major similarities, and combined use in practice. The 3D structure assessment is specified for volume fraction, V_V, specific surface area, S_V, and total lineal extension per unit of volume, L_V. Such descriptive parameters refer to the content and specific surface area of grains and pores, to the extent of damage, and to lineal density of reinforcing fibres. Elaborated examples are presented dealing with the same material features.

Keywords: Concrete technology; Gradient structure; Methodology; Stereology

1. Introduction

The awareness that behaviour of elements of cementitious materials is intimately related to material structure has grown steadily over the past several decades. However, the necessary supplementing of studies on material behaviour by thorough evaluations of material structure is not generally performed. An obvious reason is the time-consuming character of such studies. Moreover, the relatively low unit cost of the material does not form a strong impetus for doing this type of research.

Even so, studies of material structure have been performed, such as the mesolevel assessment of the actual dispersion characteristics of steel fibres in concrete. Particularly, filling of the mould and the compaction procedure induce segregation and anisometry in the fibre structure in concrete [1–3]. Further, studies have been focusing on damage evolution in concrete due to internal and external loadings. More specifically, cracking, as a fractal-like phenomenon, can be studied on different levels of the microstructure, as functions of load characteristics, or of variations in technological parameters. Therefore, meso-structural as well as micro-structural approaches are of interest. Typical examples can be found in [4–6]. TEM, SEM or optical microscopes accomplish sufficient magnification in the studies of microstructure. These latter examples also encompass porosity studies.

In all these cases, the researcher is confronted with 2D information in the form of images. Hence, information is lost, since material structure is of 3D nature. In particulate materials we can expect *geometry* to be a relevant scientific discipline that is at the basis of structure formation, and should consequently also be considered crucial for structure description. In ordered materials (crystals), geometry would suffice relating 2D observations to features of 3D material structure. For achieving this goal in disordered materials, we additionally need *probability theory*. Hence, in concrete technology one should expect *geometrical probability theory* (=stereology) to provide for the necessary quantitative image analysis tools. Examples of such approaches are unfortunately still scarce, however some exist [7–11]. Automation offers some help, but unfortunately may introduce serious biases [12,13]. A major tool nowadays is computer simulation of material structure. Realistic set ups (like those available at NIST [14,15] and DUT [16,17], based on concurrent algorithms) are a prerequisite, however, for approaching dense random packing

* Corresponding author. Tel.: +31 15 278 2307; fax: +31 15 278 8162.
E-mail address: P.Stroeven@tudelft.nl (P. Stroeven).

0958-9465/$ - see front matter © 2006 Published by Elsevier Ltd.
doi:10.1016/j.cemconcomp.2006.10.002

situations, underlying aspects of material performance that depend not only on material density.

Up to this point, we have briefly discussed how to obtain global 3D information from 2D images. Global was interpreted as the result of an averaging over sufficient large sample areas to yield representative information on the actual material. But inherently included was also the engineering aim for "bulk" information. All relevant problems arising from external boundaries (mould), or internal rigid surfaces (reinforcement, aggregate grains), or just from macro-effects like differential settlements (of fibres) or unevenly distributed stresses (due to cracking) ask the researcher to make an extra step. In some cases, the "bulk" solution can be obtained by removal of disturbed boundary layers, or by averaging procedures. In the case of macro-gradients, this solution is irrelevant. The same holds for micro-gradients, such as in the ITZ, when interested in more than local density or porosity. Hence, the researcher should know how to proceed with stereological procedures in case of gradient structures. This paper is meant to be an introduction to this field.

2. Gradient structures

Gradient structures manifest inhomogeneity in one direction and mostly homogeneity perpendicular to this direction. Here, homogeneity should be considered in stochastic sense. It requires averaging over sample space of sufficiently large linear dimensions. Bulk information in which concrete technologists are interested is mostly in terms of the structural parameters V_V, S_V, and L_V. These parameters denote volume fraction (e.g., of pores, particles), specific surface area (e.g., of cracks, pores), and length (e.g., fibre) per unit of volume, respectively. Of course, additional parameters could be of interest, such as number density (N_V), or average size ($\bar{d}$).

We consider an element of concrete equipped with an orthogonal coordinate system $\{x,y,z\}$ with the z-axis in the gradient direction as sketched in Fig. 1. Due to the homogeneity assumed in $\{x,y\}$-planes, we deal with rotational symmetry. This is a suitable model for treating most occurring cases in concrete technology. The correct approach would be to produce a so-called *vertical section* (or a series of stochastically independent vertical sections) of the element. A vertical section is a randomly selected section parallel to the z-axis, for convenience reasons denoted here as $\{x,z\}$-plane. The intuitive progress would be to approach the material as consisting of relatively thin homogeneous layers perpendicular to the z-axis, so that the $\{x,z\}$-plane reveals a system of parallel strips with a thickness Δz. The strip thickness is of course a compromise between crudeness of approximation (economy) and information supply.

Horizontal planes should be avoided because of technical reasons (making equidistant parallel sections is complicated) and because of fundamental objections: they never contain enough 2D information to make the extrapolation step to 3D reality [18]. Data acquisition procedures from here on can be simplified by adopting the Saltikov–Stroeven approximation for material structure. The general principle is that the real dispersion of elements (pores, cracks, fibres) in concrete can be replaced by a mixture of different portions of which one is ideally IUR (isotropic uniformly random), and two consist of elements randomly dispersed to a location, but in one portion all parallel to the so-called orientation plane (2D portion), and in the other one parallel to the orientation axis (1D portion). This system has been employed successfully by this author for analysis of cracks and fibres in concrete [19–22]. The most general case is the *partially linear-planar system*.

3. Partially linear-planar dispersion model

The advantage of the partially linear-planar dispersion model is that the correlations between the 2D features in section (or projection) planes and the 3D reality of the different portions can be established unambiguously, without the demand for *random sectioning*. This would be complicated and thus expensive. The basic principle behind the derivation of formulas is that the probability of a single dispersed element (fibre, crack) to intersect with a vertical plane depends on the size of the projection (length or area) perpendicular to the plane. The average projected area or length therefore governs the intersection probability of the complete portion. The average fibre length in the 1D set is taken as unity. Obviously, the projection to a plane perpendicular to the fibre direction is also unity. Intersecting the 1D fibre set with a plane in the direction of the fibre

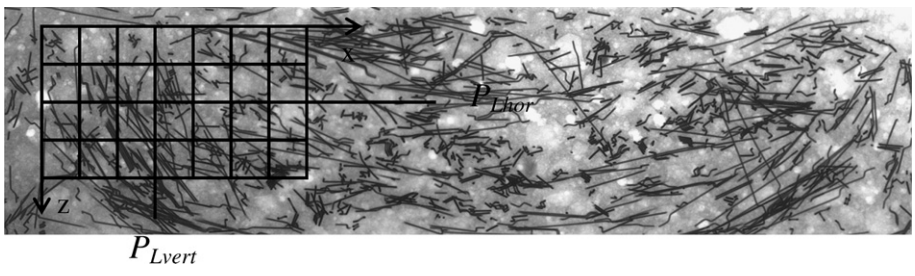

Fig. 1. Prismatic concrete specimen revealing gradient in structural parameter (L_V) in the z-direction. The specimen is supposed homogeneous in the $\{x,y\}$-plane. Shown is projection image of vertical slice of Fig. 14.

leads to zero intersections, because projected length on a plane perpendicular to the fibres is zero.

In the 2D set, average fibre length is again taken as unity. A plane perpendicular to this 2D set intersects with the fibres in proportion to their average projected length perpendicular to this plane. This is $2/\pi$, because

$$\frac{\int_0^{\pi/2}\cos\theta\,\mathrm{d}\theta}{\int_0^{\pi/2}\mathrm{d}\theta}=\frac{2}{\pi} \tag{1}$$

The angle θ is associated with the orientation of a single fibre in the orientation plane. Of course, a plane parallel to the 2D fibre portion does not intersect at all with the fibres. The average fibre length in the 3D portion is – as before – taken as unity. The average projected length of these fibres in a direction perpendicular to a randomly selected plane is 1/2, because

$$\frac{\int_0^{\pi/2}\sin\theta\cos\theta\,\mathrm{d}\theta}{\int_0^{\pi/2}\sin\theta\,\mathrm{d}\theta}=\frac{1}{2} \tag{2}$$

This allows formulating the relationships between observations in the Cartesian coordinate planes and the three independent fibre portions. It is readily found that

$$P_{Ax}=\frac{1}{2}L_{V3}+\frac{2}{\pi}L_{V2}+L_{V1} \tag{3}$$

$$P_{Ay}=\frac{1}{2}L_{V3}+\frac{2}{\pi}L_{V2} \tag{4}$$

$$P_{Az}=\frac{1}{2}L_{V3} \tag{5}$$

whereby arbitrarily the $\{x,y\}$-plane is associated with the orientation plane, and the z-axis is assumed to be the orientation axis. P_{Ax} stands for the number of fibre intersections in the $\{y,z\}$-plane per unit of area. The situation is sketched in Fig. 2. For actual fibre systems, mostly $L_{V1}\approx 0$, leading to the *partially planar system* for which Eqs. (3)–(5) are valid. We see that an orthogonal system of observation planes is required for the determination of the two unknown fibre portions. This would hold equally for bulk as for gradient values!

X-ray images can be produced in the orthrip directions. These images are superimposed by a grid of parallel lines in both of the coordinate directions. For the partially planar case, two coordinate planes and two orthogonal grid orientations will yield four observations. The following relationships are readily obtained:

$$P'_{Lz}(x)=P'_{Lz}(y)=P'_{Lx}(z)=\left(\frac{1}{2}L_{V3}+\frac{2}{\pi}L_{V2}\right)t \tag{6}$$

$$P'_{Lx}(y)=\frac{1}{2}(L_{V3})t \tag{7}$$

Herein, $P'_{Lx}(y)$ defines the number of intersections per unit of grid line length in the projection plane X-rayed in x-direction (P'_{Lx}) with the grid in horizontal (y-)direction. The thickness of the X-rayed slice is defined by t. We see that the vertical projection plane (here, x-plane), yields two independent measurements that can be used in the bulk and boundary case of fibre reinforced concrete for the determination of either L_{V3} and L_{V2}, or $L_{V3}(z)$ and $L_{V2}(z)$ in the case of a structural gradient. An example is presented in Fig. 3.

Similar correlations are available for section images of damaged concrete analyzed by a superimposed grid. Formulas for the most general case have been published earlier [20,21]. Fortunately, $S_{V2}\approx 0$ in many practical cases, leading to the *partially linear system* with the 1D portion encompassing (parts of) cracks parallel to the orientation axis. The direct compression case can be modelled by this system [18,19]. Alternatively, in some cases, $S_{V1}\approx 0$, yield the *partially planar system*. The 2D portion encompasses (parts of) cracks parallel to the orientation plane. This system suits to model the direct tensile loading case, whereby the orientation plane is perpendicular to the loading direction [1]. For the partially linear case that has relevance for shrinkage cracking at a free surface of concrete, we have

$$P_{Lx}(y)=\frac{1}{2}S_{V3}+\frac{2}{\pi}S_{V1}=P_{Ly}(x) \tag{8}$$

$$P_{Lx}(z)=\frac{1}{2}S_{V3}=P_{Lz}(x)=P_{Lz}(y) \tag{9}$$

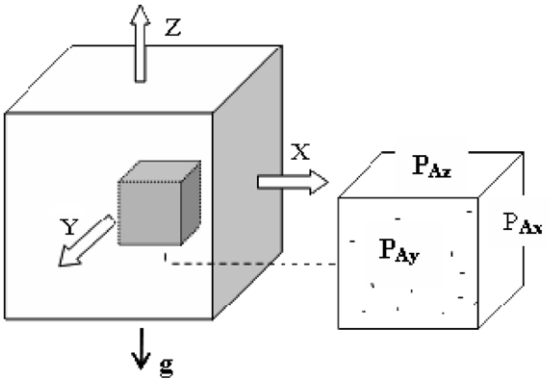

Fig. 2. Prismatic specimen of SFRC subjected to orthip sampling, whereby the three orthogonal sections are subjected to feature counting.

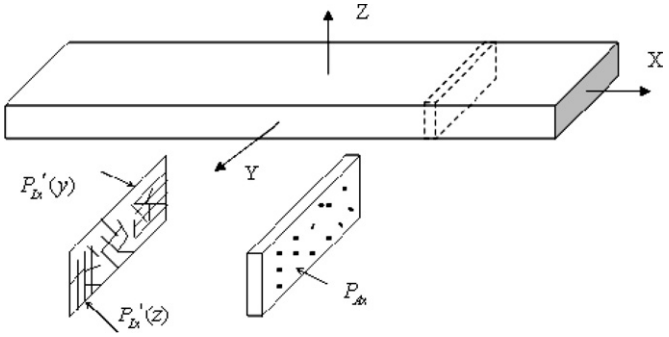

Fig. 3. Projection (bottom left) and section (bottom right) images of vertical slice of SFRC specimen (top) subjected to counting operations (see also Fig. 1).

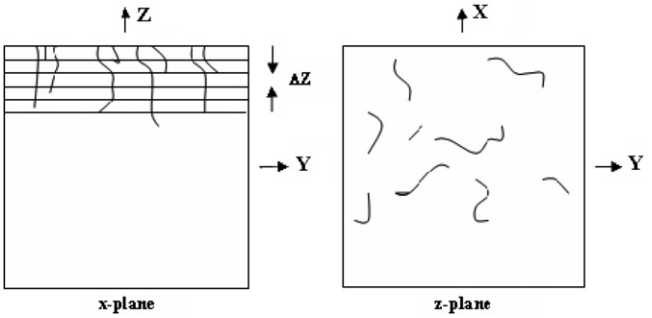

Fig. 4. Image of *vertical section* (left) of cracked concrete specimen subjected to intersection counting by a grid. For complete analysis the grid should be placed in orthogonal directions.

Herein, $P_{Lx}(z)$ defines the number of intersections per unit of grid line length in the x-plane analyzed by a grid in the vertical (z)-direction. Obviously, a single vertical section provides two independent observations in orthogonal positions of the grid system ($P_{Lx}(y)$ and $P_{Lx}(z)$, or $P_{Ly}(x)$ and $P_{Ly}(z)$) that can be used to solve the bulk or boundary problem. The situation is sketched in Fig. 4.

4. Methodology in gradient cases

The estimation of the gradient structure in volume fraction, $V_V(z)$, is straightforward, because of its equality with areal fraction. This can be quantified in homogenized strips by the lineal analysis of Rosiwal [23] or by point counting [24,25].

Determination of specific surface area (of particles, cracks, pores) in the literature is treated as the bulk case applied to the homogenized strips. The appropriate formula is

$$S_V(z) = \frac{4}{\pi}\overline{L}_A(z) = 2\overline{P}_L(z) \tag{10}$$

Application requires *orientational randomization*, a cumbersome operation in concrete technology. Under the assumptions of homogeneity in $\{x,y\}$-planes, it has been demonstrated, nevertheless, that but a vertical section has to be analysed. However, a regular pattern of cycloids should be employed instead of a lineal grid. In doing so, the intersection density with the lineal features (cracks, pores, particle perimeters) can be determined. This approach accounts for the sine weighed sampling requirement in space [26,27]. The same approach could be followed in case of the homogenized strips. However, great care should be bestowed on the generation process of the cycloids [28].

Once the Saltikov–Stroeven concept of the partially linear-planar system is adopted for bulk applications, it can equally be employed for gradient investigations, avoiding the requirement of orientational randomization. The example of shrinkage cracking at the free surface [29] will be discussed. This leads to gradient cracking structures perpendicular to the free surface, supposedly the z-direction. Hence, Eqs. (8) and (9) are valid. The homogenized strips in the vertical x-plane should be subjected to intersection counting in horizontal (y) as well as vertical (z) directions. Eq. (9) will yield minor contributions since cracks predominantly run in the z-direction, so series of *stochastically independent vertical sections* will be required for obtaining reliable estimates.

A new method proposed in [30] is based on line scanning in horizontal direction *only*. The scanning line is superimposed halfway the vertical strips. The estimate of $S_V(z)$ is obtained from

$$S_V(z) = \frac{1}{L}\sum_{i=1}^{n}(\alpha_i + \cot\alpha_i) = \frac{1}{L}\sum_{i=1}^{n}\left(\alpha_i + \frac{L'_i}{\Delta z}\right) \tag{11}$$

in which α_i is the angle between the scanning line and the crack, L'_i is the projected length of the part of the crack inside the slice on the scanning line, and Δz is the width of the strip, and L is the length of the scanning line inside the slice, as shown in Fig. 5.

Gradient fibre structures in X-ray projection images require determination of $L_V(z)$, the total fibre length per unit of volume as a function of z. The alternative of Eq. (10) for the bulk case is:

$$L_V = \frac{4}{\pi}t\overline{L}'_A = 2t\overline{P}'_L \tag{12}$$

with t as the slice thickness, $\overline{L}'_A$ as the total fibre projected length per unit of area, and $\overline{P}'_L$ as the number of intersections per unit of grid line length in the projection plane. The bar on top of the parameters implies a process of *orientational randomization.* This is uneconomic and has practical drawbacks. Generally, the solution is obtained on *vertical slices* (parallel to the compaction direction), whereby homogeneity is assumed perpendicular to this axis. A superimposed grid of oriented cycloids can be used for counting intersections with the fibre projections [30]. The shape of the cycloid accounts for the sine-weighing factor in space.

The Saltikov–Stroeven approach is equally possible, however. The most general situation of a partially linear-planar structure can be adopted. For relevant formulas, see [31]. In most cases, the partially planar model would be a suitable approximation, reducing efforts significantly. So, it would be the best value for money.

The approach follows similar procedures as for specific surface area. Hence, the unknowns are L_{V3} and L_{V2}. When

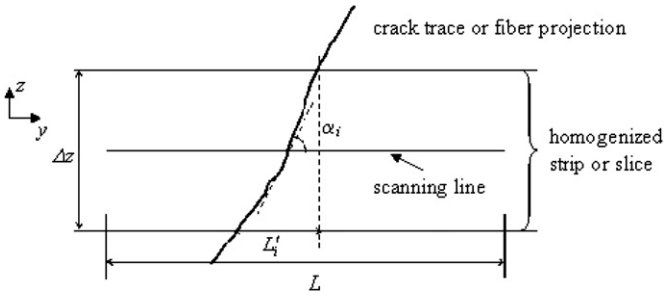

Fig. 5. Gradient in specific surface area in vertical (z) direction assessed by single line scanning perpendicular to the gradient direction (y-direction).

an orthogonal grid is superimposed on the vertical projection image in an orthogonal system with the z-axis as the compaction direction, we have

$$P'_{Ly}(x) = \frac{1}{2}\frac{L_{V3}}{t} \tag{13}$$

$$P'_{Ly}(z) = \frac{1}{2}\frac{L_{V3}}{t} + \frac{2}{\pi}\frac{L_{V2}}{t} \tag{14}$$

$P'_{Ly}(z)$ represents the number of intersections in the projection plane of the vertical slice (y-plane) with a grid of parallel lines in the z-direction. The X-ray radiograph of the horizontal slice will show a non-directional system that can be sampled in arbitrary direction by a directed line grid. Measurements would be governed by Eq. (14), so that the general solution can never be based on a horizontal slice only. Contrarily, combination of Eqs. (13) and (14) will provide the general solution

$$L_{V2} = \frac{\pi}{2t}\{P'_{Ly}(z) - P'_{Ly}(x)\} \tag{15}$$

$$L_{V3} = \frac{2}{t}P'_{Ly}(x) \tag{16}$$

$$L_V = L_{V2} + L_{V3} = \frac{\pi}{2t}\left\{P'_{Ly}(z) + \left(\frac{4}{\pi} - 1\right)P'_{Ly}(x)\right\} \tag{17}$$

Conventionally, the ratio of Eqs. (15) and (17) is defined as the *spatial degree of orientation*, ω_3, of the fibres in concrete.

Basically, the same set up can be employed in the case of a gradient structure, whereby narrow strips of constant width are defined on the radiograph perpendicular to the gradient direction.

The alternative of Eq. (11), only requiring line sampling perpendicular to the gradient direction is

$$L_V(z) = \frac{1}{tL}\sum_{i=1}^{n}\left\{1 + \left(\frac{\pi}{2} - \alpha_i\right)\cot\alpha_i\right\} = \frac{1}{tL}\sum_{i=1}^{n}\left\{1 + \left(\frac{\pi}{2} - \alpha_i\right)\frac{L'_i}{\Delta z}\right\} \tag{18}$$

The method based on Eqs. (11) and (18) requires measurement of the angle between structural features in the image plane (cracks in section and fibre projections in radiograph) and the scanning line. Automation can be accomplished [30].

5. Applications to gradient structures

5.1. Gradient structure in V_V of particles and pores in concrete

5.1.1. Gradient in volume fraction of aggregate

This is the least complicated of gradient structures, as stipulated earlier. Common practice in materials research is the removal of the so-called disturbed boundary zone, allowing for observations on *bulk* material, and recording of bulk performance. The thickness of this layer is generally assumed as a function of maximum grain size only, although long-range gradients in volume fraction can occur. An example will be presented revealing the gradient to extend over full specimen dimensions. Use was made of 250×350 mm prisms in experiments of which a single example will be presented. For further information, see [26,33]. Mono-size ceramic spheres (16 mm) replaced the largest grain size fraction of a conventional aggregate. Mixes were produced with three different volume fractions of this material (design values of 0.10, 0.23 and 0.37 of the aggregate). Boundary layers of 25 mm thick were removed on all sides (about 1.5 times maximum grain size), yielding 200×300 mm prisms of "bulk" material. The prisms were serially sectioned over their height, resulting in tiles of $200 \times 200 \times 11$ mm, providing 38 square images with 200 mm side length. Typical images of the three mixtures are displayed in Fig. 6. These sections replaced the homogenized strips (4 times 11×200 mm) that offer qualitatively similar information but with increased scatter.

The images were subjected to areal, lineal and point counting analyses for assessment of estimates of volume fraction of the 16 mm grain fraction over the height of the prisms. This allowed comparison of efficiency (degree of scatter) of the methods. Since the ceramic spheres were added without modifications of the rest of the mixture, workability (slump values) were high, medium and low for the respective concretes with increasing amount of ceramic aggregate fraction. The consequences are reflected by the gradients in V_V over the height of the bulk concrete prisms shown in Fig. 7. The low-volume of coarse aggregate mixture reveals *segregation* in the coarse aggregate, whereas the *boundary effect* extends over the full height in the high-volume case.

5.1.2. Porosity gradient in the ITZ

Another example is taken from computer simulation approaches to study density gradients of cement particles in the ITZ around aggregate particles. Fig. 8 is obtained by SPACE system that uses a concurrent algorithm for generating densely packed particulate materials [16,17,34]. The *experimental design* is always based on the concept of homogenized strips parallel to the perimeter of the aggregate's grain section [35–37]. Unfortunately, the image plane is never perpendicular to the grain surface, so that biased (too low) values are obtained for the slope of the ITZ's gradient structure (because its thickness is overestimated) [38]. In the computer simulation approach, the sections parallel to the grain surface can be used for estimating V_V. The advantage over the homogenized strips is the same as in the previous example. Note that porosity is the reciprocal value of particle density in Fig. 8.

5.2. Gradient structure in S_V of shrinkage cracks in concrete

The example deals with damage due to shrinkage at a free surface, which allows defining an axis of symmetry.

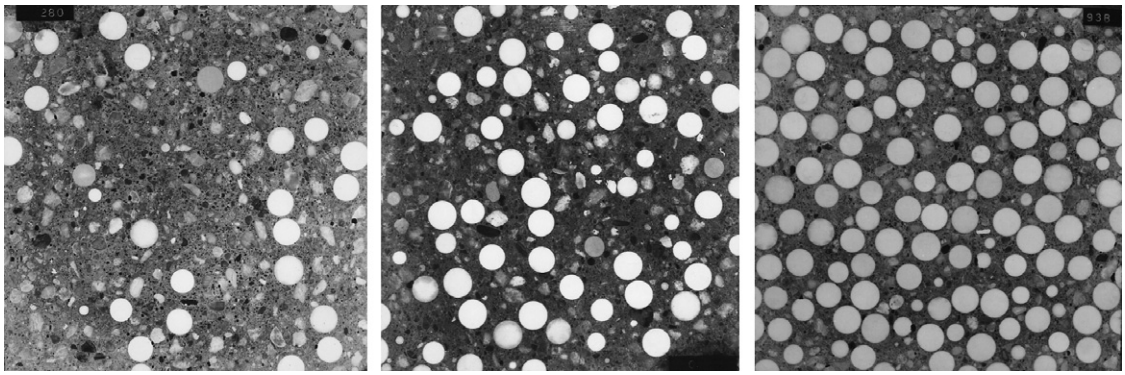

Fig. 6. Images (200 × 200 mm) of horizontal sections (replacing the strips in the vertical section) of three mixtures of concretes with different amounts of mono-size ceramic balls as 16 mm maximum aggregate.

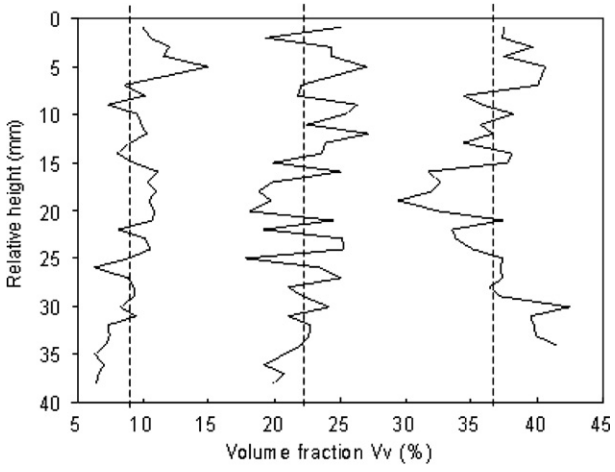

Fig. 7. Gradient structures in V_V of mixtures with different amounts of coarse ceramic aggregate (viz., Fig. 6). The dashed lines indicate the respective values of volume fraction. The top of the specimen is situated at the bottom of the scale.

The images to which the quantitative image analysis approach is applied are due to Bisschop (produced in the framework of his Ph.D. study [29]). He studied the effect of size (0.5, 1, 2, 4, and 6 mm) and volume fraction (10, 21, and 35%) of mono-size spherical glass aggregate on shrinkage performance of prismatic specimens (40 × 40 × 160 mm) of which one surface (40 × 160 mm) was exposed to the environment. Specimens were seven days old when exposed to 30% RH and 30 °C. Fluorescent epoxy impregnation was employed for stabilizing the crack structure in the central 63 mm long portion of the prisms. Four vertical sections were made 9 mm and 16 mm from the nearest surface. Crack patterns were mapped manually at 40× magnification. *Digitised* crack maps of the four vertical sections of a single specimen were superimposed before being analysed by OPTIMAS image analysis software. Reports of the findings can be found in [29] and in further publications (e.g., [6]). Among other things, total global 2D crack length and marginal orientation distribution were assessed as function of the glass marble aggregate characteristics. Unfortunately, it is proven as impossible deriving unbiased crack length and orientation distribution from digitised images [13,18]. Other biases are introduced by keeping the size of images constant while changing maximum aggregate size, leading to different sizes of representative volume/area elements [18,39]. We will therefore only consider the effect of aggregate volume density, and perform the analysis manually. Results of the global (bulk)

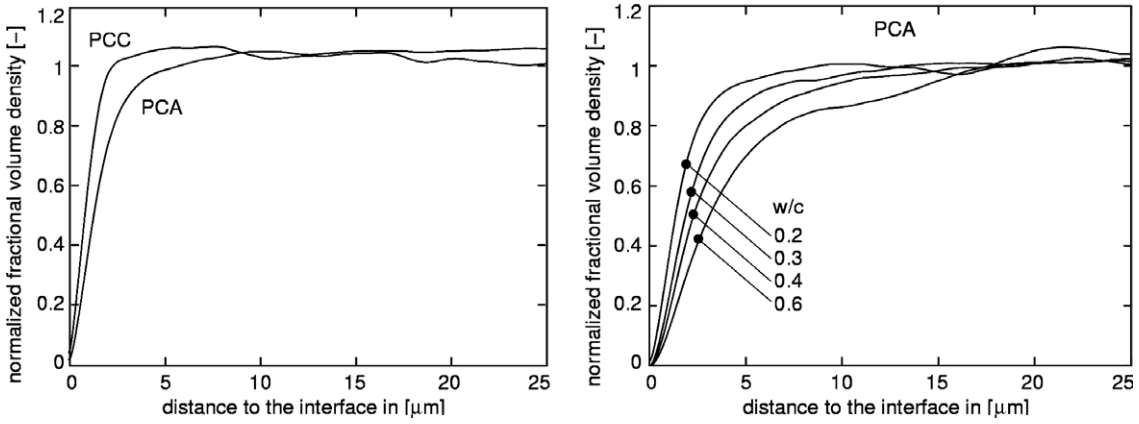

Fig. 8. Effect of cement fineness (left) and water to cement ratio (right) on the gradient structures of volume-based cement particle density in the ITZ (reciprocal value is porosity).

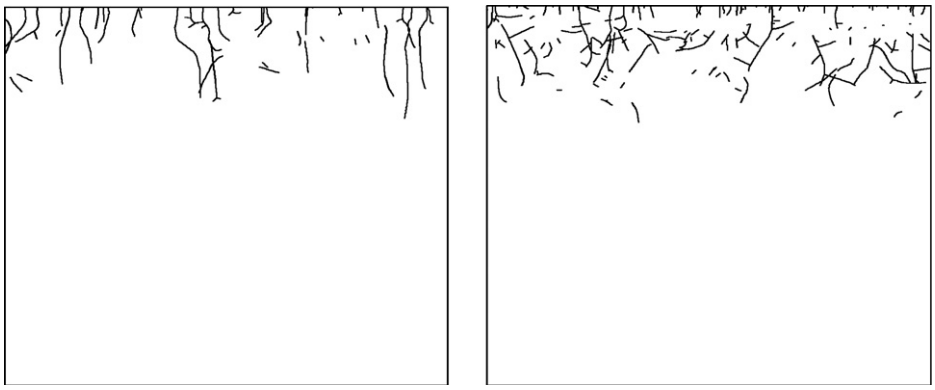

Fig. 9. Both images consist of superimposed shrinkage crack patterns of four vertical sections. They are subjected to directed secants approach for assessment of global information. Volume fraction of 4 mm glass balls involved is 10% (left) and 35% (right), respectively [29].

approach will be presented additionally, because together a good insight can be obtained in damage evolution due to shrinkage cracking at a free surface. Additionally, information becomes available for assessment of inherent biases in the methodology adopted in [6,29].

A grid with 60 parallel lines was superimposed on the sample image of 40×40 mm, covering in the 90° directions by far the major part of the width of the cover zone in the image (Fig. 9). This grid was successively superimposed in 0, 30, 60, 90, 120 and 150° orientations on the *same area*. Table 1 presents the global data of the directed secants analysis on free shrinkage cracking for concrete specimens containing different amounts of 4 mm mono-size glass spheres.

The approach in [6,29] was based on four-connexity digitised images. Equally oriented line elements were added and plotted in a polar figure, $L'(\theta)$, the so-called radar diagram. An example is presented in Fig. 10a pertaining to the composite sample with aggregate volume fraction of 21%. Fig. 10b is the rose of the number of intersections of the same image (based on the data in Table 1). The radar diagram presents *average* values of the four images, so for comparison reasons the radar values should be multiplied with the factor four to obtain total crack length in one of the four directions in the crack images. As can be seen, radar values offer a biased impression on crack orientation and length. Moreover, the roses can offer more detailed insight into the crack orientation distribution. Finally,

Table 1
Directed secants analysis of free shrinkage cracking

Volume fraction (%)	Number of intersections for grid orientations					
	0°	30°	60°	90°	120°	150°
0	144	128	80	26	–	–
10	184	155	109	59	108	165
21	222	206	170	132	163	214
35	220	213	176	163	192	224

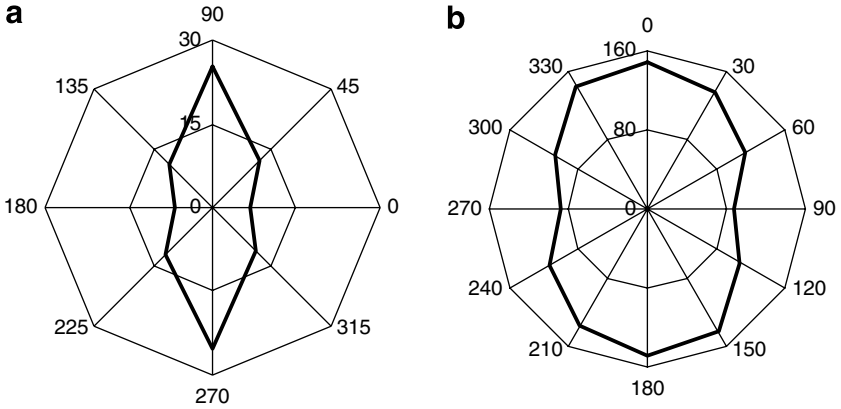

Fig. 10. Orientation distribution of crack length in mm: (a) radar diagram based on automated analysis of four-connexity digitized image (constructed from the data presented in [6]), (b) rose of crack extension orientation of the same image of mortar with 21% 4 mm glass marble aggregate ($P_L(\theta)A = L'(\theta + \pi/2)$). Note that the rose has been rotated 90° to be directly comparable with the radar diagram.

the stereological approach yields (or can yield) three-dimensional structural information.

Linear value of crack tortuosity is calculated by the expression

$$R_l = \frac{\pi}{2}\frac{\overline{P}}{P(0)} \tag{19}$$

with $\overline{P}$ is the average number of intersections for the six different orientation directions of the directed secants, and $P(0)$ is the number of intersections for zero degree orientation of the directed secants with unit line spacing ($\Delta a = 1$). This relationship is based on Cauchy's expression for total crack length, L [32]

$$L = \frac{\pi}{2}\overline{P}\Delta a \tag{20}$$

The global calculation results of the degree of orientation (=oriented divided by total crack surface area), crack tortuosity, and total crack length are collected in Table 2.

To get information on the *gradient structure*, an orthogonal grid was superimposed on the same images. The grid formed 6×26 small squares in the cracked boundary zone of the free shrinkage specimen (the same as used for the sweeping test line application). An example is presented in Fig. 11. To keep the analysed area similar, minor cracking extended in some cases outside this region. Fig. 12 presents the data obtained by application of Eqs. (8) and (9).

A global average value had to be used for the intersection density in vertical direction, due to the limited information provided by the restricted sample area. The images with shrinkage cracks subjected to the quantitative image analysis were magnified by a factor of 2.75. The linear dimension of the squares formed by the grid would amount to 1.47 mm on the real section of 40 × 40 mm. This scale factor is used for the calculation of the values of the specific crack surface area in Fig. 12 and Table 3. This table gives the global values of 3D and 1D components of the specific surface area of shrinkage cracking, and – as an example – also the values of the first (outer) strip only. The presented three-dimensional global and gradient information on shrinkage cracking at a free surface offers able possibilities for describing the process characteristics of damage evolution. Sample size was insufficient, leading to larger scatter in data [6,29]. The image of the 21% aggregate composite (four superimposed serial sections) contains

Table 2
Characteristics of free shrinkage cracking

Volume fraction (%)	Degree of orientation ω_3 (%)	Tortuosity R_l	Total crack length L (mm)
0	78.1	1.03	133
10	62.5	1.11	182
21	34.9	1.31	259
35	14.0	1.41	276

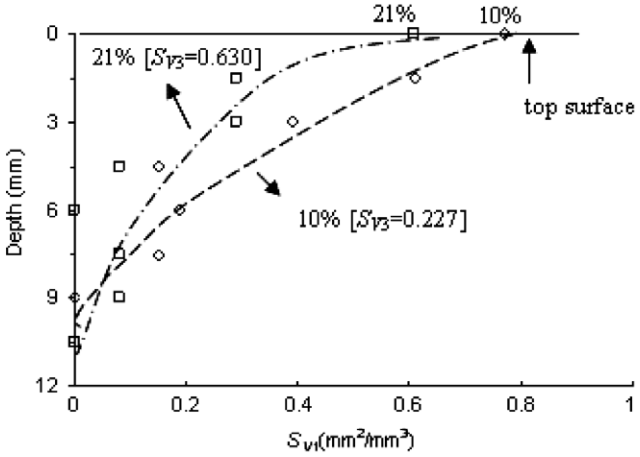

Fig. 12. 1D component (S_{V1}) in specific surface area of shrinkage cracks as a function of depth under the free surface. Gradient structures of S_{V1} for mortars with 10% and 21% by volume of 4 mm glass balls as maximum aggregate are presented.

Table 3
Orthogonal grid analysis of free shrinkage cracking; subscript e stands for the external surface layer (1/6th of the cracked depth) only

Specific crack surface area (mm²/mm³)	Aggregate volume fraction (%)		
	10	21	35
S_{V1}	0.327	0.157	0.253
S_{V3}	0.227	0.630	0.604
S_V	0.554	0.787	0.857
S_{V1e}	0.573	1.036	0.962
S_{V3e}	0.059	0.093	0.084
S_{Ve}	0.632	1.129	1.046

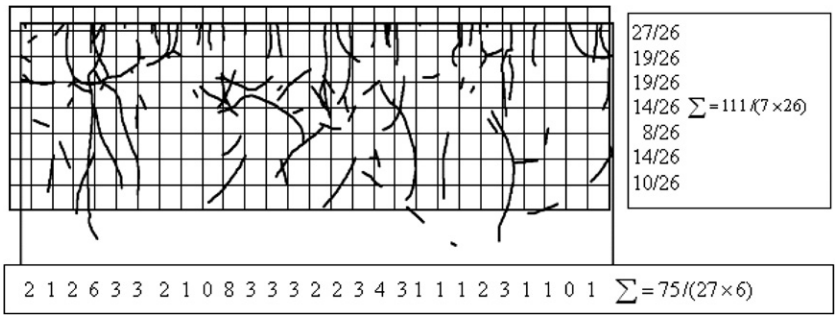

Fig. 11. Example of intersection counting by orthogonal grid. Image represents mortar containing 21% by volume of 4 mm glass balls as maximum aggregate. Image is superposition of four vertical sections, as in Fig. 9. Note that grid position is not necessarily precisely the same as in the experiment.

about 75–80 crack traces. The linear spacing of the square line grid was optimized according to the rule of thumb implying the number of intersections to roughly equal the number of crack traces. So, coefficient of variation in the number of intersections will be around 10–12%. S_{V3}-values in Table 3 will be accurate to about this level, but in the case of the S_{V1}-values, variation will be twice as large. The data in Table 2 were obtained at smaller line spacing, leading to a coefficient of variation of about 7% in the $P(\theta)$-values in Table 1. The accuracy of the nominator is high [32], say 1.5–2%. Hence, the denominator governs the accuracy of crack tortuosity in Table 2. Tortuosity values will therefore be accurate to about 10%. Accuracy of the degree of orientation, ω, will be much lower, but differences between the values for the different composites are still significant.

5.3. Gradient structure in L_V of steel fibres in concrete

Results of extensive experimental studies on fibre distribution in SFRC have been reported elsewhere [1,40]. Twelve concrete slabs were cast for the experiments. Each slab represents a particular concrete mixture, either plain or steel fibre reinforced. Standard aggregate grading with 8 mm maximum grain size, an ASTM Type I Portland cement of 375 kg/m^3, and a water/cement ratio of 0.5 were applied. Plain steel fibres (25×0.38 mm) were added in six different volume contents between 0.5 and 3%. Superplasticizer content (0–2%) and vibration times (0–180 s) were also varied. Six prisms ($100 \times 100 \times 500$ mm) were cut from each slab.

Prisms were subjected to four-point bending tests, and thereupon cut into cubes for splitting tensile testing. Further, various section images in orthrip directions were prepared per prism, yielding a total of about 300 section images of 100×100 mm. All section images were subdivided in eight homogenized strips (of 12.5 mm width). This is in agreement with an analytical approach demonstrating the thickness of the boundary zone to equal half the fibre length [40]. When relevant, the strips were taken perpendicular to the gravitation direction in the plate during compaction. In all strips, the numbers of fibres were determined.

All vertical sections showed a combination of *segregation* and a *boundary effect* in the number of fibres (and, of course, also in intersection densities). The discrete strip values could be approximated per image by a second order parabola, as demonstrated in Fig. 13, allowing to quantitatively distinguishing between segregation (S) and boundary effect (B). For transformation of the intersection density, P_A, to three-dimensional quantities, use is made of Eqs.

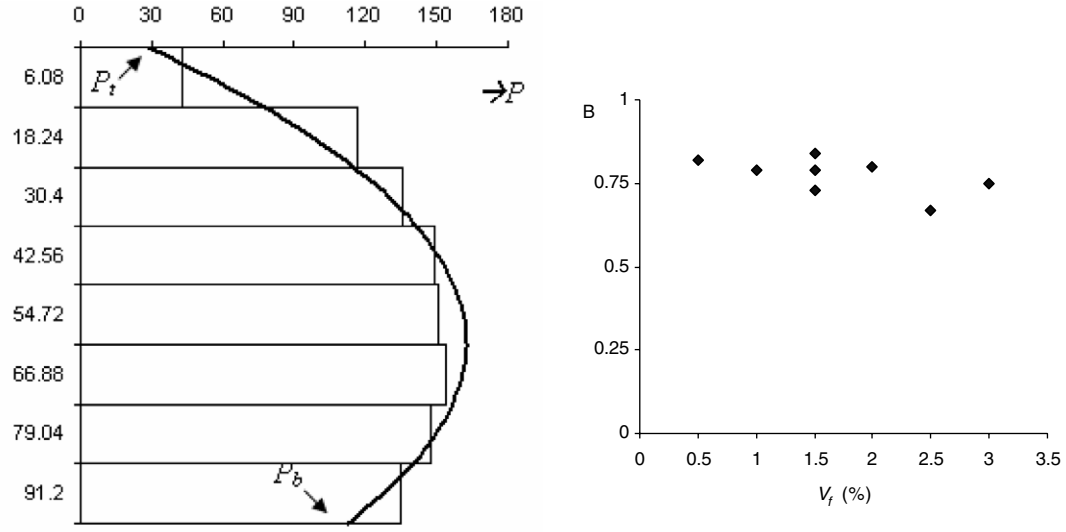

Fig. 13. Gradient structure in number of fibres in gravitation direction for vertical section of SFRC prism (left). At the right, the boundary effect ($B = (P_b + P_t)/2\overline{P}$) is shown depending marginally on the fibre content.

Fig. 14. Location of vertical slices prepared of prismatic steel fibre reinforced concrete specimen ($1000 \times 200 \times 50$ mm). X-ray radiographs were prepared of all slices (an example is shown in Fig. 1), and intersection counting was performed with an orthogonal grid. Homogenized strips would allow estimating gradient structures in 2D and 3D components of fibre dispersion.

(3)–(5). That is, homogenized data are derived from orthogonal sections and combined with the gradient values, so that the three equations can be solved for the three unknown fibre fractions.

In another extensive program, the gradient structure analysis was performed on X-ray projection images. Prismatic specimens of $50 \times 200 \times 1000$ mm were prepared, three per parameter combination. The experiments encompassed 1.73% by volume of three different steel fibre types (plain, hooked and paddled) and four types of concrete matrices (w/c ratios of 0.4 and 0.6, and two different values of aggregate grading) with 8 mm maximum grain size. Specimens were subjected to direct tensile stresses in a servo-controlled machine. The specimens were X-rayed over their full thickness before testing. After the test, the specimens were cut into regular pieces, yielding 10 roughly equally spaced vertical slices, as revealed by Fig. 14. X-ray radiographs were also produced of these slices.

All vertical images (radiographs of vertical slices) reveal fibre segregation (more apparent for the larger fibre type) and boundary effects, as can be observed in Fig. 1. The quantification should be by way of homogenized strips over the height of the projection image, and counting intersections in orthogonal positions of a grid of straight, equidistant lines that is also shown in Fig. 1. Use can be made of Eqs. (6) and (7) for determination of two fibre portions in a partially planar system.

6. Discussion

Assessment of relevant geometric properties of gradients structures in cementitious systems requires significant time investments and hard work, inherent to all quantitative image analysis approaches. On the other hand, we deal with simple types of observations. Still, whether it is worth the efforts will depend on the situation. In the first place, the relevant scene is that of experimental laboratory *research*. In the second place, we may be confronted with weak gradient structures, such as that met with steel fibre reinforcement in specimens. The neglect to assess the reinforcement details near the external surface will cause a modest decline in reliability of the global mechanical estimates, which are only partly influenced by the possible slight decline in fibre reinforcement near the external surface of the specimen. However, we may also be confronted with very strong gradient structures, such as that met with porosity in matured cement paste. It was found that the near presence of rigid surfaces from aggregate grains significantly influenced the total porosity gradient in the cement pockets in the hardening material. Even more dramatic were the gradient details in the *continuous porosity* [41]. Ignorance of these gradient details and only recording global continuous porosity data would lead to completely *irrelevant* pore network modeling approaches for durability purposes. So, assessment of the geometric details of the pore gradient structure would be a serious job. The outcomes will govern both relevance and reliability of durability studies that proceed from such details.

7. Conclusions

Plain or fibre reinforced cementitious materials, once moulded, reveal gradients on various levels of the microstructure. The descriptive parameters of prime importance are volume fraction, V_V, specific surface (or crack) area, S_V, and total length (of fibres) per unit of area, L_V. The proper stereological approach to bulk analysis on so-called vertical sections is briefly presented. This is shown revealing a practical and economic approach to provide the aforementioned three-dimensional structure information. The same concept is expanded in this paper for the so-called layered structures, i.e., structures of which the vertical sections are sub-divided into horizontal homogenized strips. This provides for an equally practical and economic, unbiased, and three-dimensional approach to gradient assessment as to the aforementioned parameters.

The methodology is based on counting intersections between the structural features of interest and a sweeping test line (or just an orthogonal system). Reference is given to a fairly new method proposed in the international literature, but the present authors have no experiences as to applications in concrete technology. Of the presented methodology, applications are presented for each of the structural features (V_V, S_V, L_V). Main purpose was to illustrate the gradient approaches; detailed information has been published earlier.

These examples demonstrated the methodology to be convenient and objective. The laborious character is inherent to structure assessment. Automation can lead to serious biases, however, as shown in this paper. So care should be bestowed on this aspect of experimental design.

Acknowledgements

The images of vertical sections (e.g., Fig. 9) obtained in shrinkage experiments, as well as the associated radar diagrams (e.g., Fig. 10a), used in this paper for illustrating the assessment methodology of gradient structure information, were provided to the first author by Dr. J. Bisschop. This is gratefully acknowledged. The present authors explicitly referred to the relevant publications focussing on these shrinkage investigations.

References

[1] Stroeven P. Micro- and macro-mechanical behaviour of steel fibre reinforced mortar in tension. Heron 1979;24(4):7–40.
[2] Stroeven P. On simulation, image analysis and structural modeling of steel fibre concrete. In: Beheshti MR, Zreik K, editors. Advanced Technologies Architecture, Planning, Civil Engineering. Amsterdam: Elsevier Science Publishers; 1993. p. 399–404.
[3] Stroeven P, Dalhuisen DH. Damage evolution characteristics of steel fibre reinforced concrete in tension. Engr Mech 1996;3(4):273–80.

[4] Stroeven P. Geometric probability approach to the examination of microcracking in plain concrete. J Mat Sc 1979;14:1141–51.
[5] Reinhardt HW, Stroeven P, den Uijl JA, Kooistra TR, Vrencken JHAM. Einfluss von Schwingbreite, Belastungshöhe und Frequenz auf die Schwingfestigkeit von Beton bei niedrigen Bruchlastwechselzahlen. Betonw & Fertigt-Techn 1978;44:498–503.
[6] Bisschop J, van Mier JGM. Effect of aggregates on drying shrinkage microcracking in cement-based composites. Mat Struct 2002;35(252):453–61.
[7] Stang H, Mobasher B, Shah SP. Quantitative damage characterization in polypropylene fibre reinforced concrete. Cem Concr Res 1990;20:540–58.
[8] Nemati KM. Generation and Interaction of Compressive Stress-Induced Microcracks in Concrete. PhD thesis. Berkeley, University of California, 1994.
[9] Ringot E. Automatic quantification of microcracks network by stereological method of total projections in mortars and concrete. Cem Concr Res 1988;18:35–43.
[10] Granju JL, Ringot E. Amorphous iron fibre reinforced concretes and mortars, comparison of the fibre arrangement. Acta Stereol 1991;10(1):113–22.
[11] Gettu R, Gardner DR, Saldívar H, Barragán. Study of the distribution and orientation of fibers in SFRC specimens. Mat Struct 2005;38:31–7.
[12] Chaix JM, Grillon F. On the rose of directions measurements on the discrete grid of an automatic image analyser. J Microsc 1996;184:208–13.
[13] Stroeven P, Stroeven AP, Dalhuisen DH. Image analysis of "natural" concrete samples by automated and manual procedures. Cem Concr Comp 2001;23:227–36.
[14] Bentz DP. Three-dimensional computer simulation of Portland cement hydration and microstructure development. J Americ Cer Soc 1997;80(1):3–21.
[15] Bentz DP, Garboczi EJ. A digitised simulation model for microstructural development. In: Mindess S, editor. Advances in Cementitious Materials. Westerville (Ohio): Amer Cer Soc; 1989. p. 211–6.
[16] Stroeven M. Discrete numerical model for the structural assessment of composite materials. PhD Thesis. Delft, Delft University Press, 1999.
[17] Stroeven P, Stroeven M. SPACE approach to concrete's space structure and its mechanical properties. Heron 2001;46(4):265–89.
[18] Stroeven P. Implications of the law of aggregation of matter in concrete technology. In: Brandt AM, Li VC, Marshall IH, editors. Brittle Matrix Composite 7. Cambridge (UK): Woodhead Publ; 2003. p. 129–42.
[19] Stroeven P. Structural characterization of steel fibre reinforced concrete. In: Brandt AM, Marshall IH, editors. Brittle Matrix Composites 2. London: Elsevier Appl Sc; 1989. p. 34–43.
[20] Stroeven P. The analysis of fibre distributions in fibre reinforced materials. J Microsc 1977;111(3):283–95.
[21] Stroeven P. Morphometry of fibre reinforced cementitious materials. Parts I. Mat Struct 1978;11(61):31–8;
Stroeven P. Morphometry of fibre reinforced cementitious materials. Part II. Mat Struct 1979;12(67):9–20.
[22] Stroeven P. Damage evolution in concrete; application of stereology to quantitative image analysis and modelling. In: Kimpara I, Kageyama K, Kagawa Y, editors. Advanced Materials for Future Industries: Needs and Seeds. Tokyo: SAMPE; 1991. p. 1436–43.
[23] Rosiwall A. Über geometrische Gesteinsanalysen. Ein einfacher Weg zur ziffermässigen Feststellung des Quantitätsverhaltnisse der Mineralbestandteile gemengter Gesteine. Verh. KK Geol Reichsanst 1898;5–6:143–75.
[24] Thomson E. Quantitative microscopic analysis. J Geol 1930;38:193–222.
[25] Glagolev AA. Quantitative analysis with the microscope by the point method. Eng Min J 1934;135:399–400.
[26] Stroeven P. Some Aspects of the Micromechanics of Concrete. PhD Thesis. Delft, Delft University of Technology, 1973.
[27] Underwood EE. Quantitative Stereology. Reading (MA): Addison-Wesley; 1970.
[28] Stroeven P, de Haan YM. Structural investigations on steel fibre reinforced concrete. In: Reinhardt HW, Naaman AE, editors. High Performance Reinforced Cement Composites. London: E&FN Spon; 1992. p. 407–18.
[29] Bisschop J. Drying shrinkage microcracking in cement-based materials. PhD Thesis. Delft, Delft University Press, 2002.
[30] Hahn U, Micheletti A, Pohlink R, Stoyan D, Wendrock H. Stereological analysis and modelling of gradient structures. J Microsc 1999;195(2):113–24.
[31] Stroeven P, Shah SP. Use of radiography-image analysis for steel fibre reinforced concrete. In: Swamy RN, editor. Testing and Test Methods of Fibre Cement Composites. Lancaster: Constr Press; 1978. p. 345–53.
[32] Kendall MG, Moran PAP. Geometric Probability. London: Butler & Tanner Ltd; 1963.
[33] Stroeven P. Stereological analysis of structural inhomogeneity and anisotropy of concrete. In: Exner HE, editor. Quantitative Analysis of Microstructures in Medicine, Biology and Materials Development, Special Issues of Practical Metallography. Stuttgart: Dr. Riederer-Verlag GmbH; 1975. p. 291–307.
[34] Williams SR, Philipse AP. Random packings of spheres and spherocylinders simulated by mechanical contraction. Phys Rev E 2003;67(051301):1–9.
[35] Scrivener KL. Characterization of the ITZ and its quantification by test methods. In: Alexander MG, editor. Engineering and Transport Zone in Cementitious Composites. RILEM report 20. ENS-Cachan: RILEM Publishing; 1999. p. 3–15.
[36] Larsen G. Microscopic point measuring: a quantitative petrographic method of determining the $Ca(OH)_2$ content of the cement paste of concrete. Mag Concr Res 1961;13(38):71–6.
[37] Diamond S, Huang J. The ITZ in concrete – a different view based on image analysis and SEM observations. Cem Concr Res 2001;23:179–188.
[38] Stroeven P. Analytical and computer-simulation approaches to the extent of the interfacial transition zone in concrete. In: Brandt AM, Li VC, Marshall IH, editors. Brittle Matrix Composites 6. Cambridge (UK): Woodhead Publishing; 2000. p. 465–84.
[39] Hu J, Stroeven P. Local porosity analysis of pore structure in cement paste. Cem Concr Res 2005;35(2):233–42.
[40] Stroeven P. Effectiveness of steel wire reinforcement in a boundary layer of concrete. Acta Stereol 1991;10(1):113–22.
[41] Chen H, Stroeven P, Ye G, Stroeven M. Influence of boundary conditions on pore percolation in model cement paste. Key Engineering Materials 2006;302/303:486–92.